AGU PUBLICATIONS

JGR

Journal of Geophysical Research: Planets

RESEARCH ARTICLE

10.1002/2014JE004678

Key Points:
- The location of Mars prime meridian has been updated
- New IAU expressions are needed for the Mars spin state and prime meridian
- Unique processing techniques and results are presented for THEMIS, HRSC, and MOLA

Correspondence to:
T. C. Duxbury,
tduxbury@gmu.edu

Citation:
Duxbury, T. C., P. Christensen, D. E. Smith, G. A. Neumann, R. L. Kirk, M. A. Caplinger, A. A. Albee, N. V. Seregina, G. Neukum, and B. A. Archinal (2014), The location of Airy-0, the Mars prime meridian reference, from stereo photogrammetric processing of THEMIS IR imaging and digital elevation data, *J. Geophys. Res. Planets*, *119*, 2471–2486, doi:10.1002/2014JE004678.

Received 18 JUN 2014
Accepted 3 NOV 2014
Accepted article online 11 NOV 2014
Published online 5 DEC 2014

The location of Airy-0, the Mars prime meridian reference, from stereo photogrammetric processing of THEMIS IR imaging and digital elevation data

T. C. Duxbury[1], P. Christensen[2], D. E. Smith[3], G. A. Neumann[4], R. L. Kirk[5], M. A. Caplinger[6], A. A. Albee[7], N. V. Seregina[1,8], G. Neukum[9], and B. A. Archinal[5]

[1]School of Physics, Astronomy and Computational Sciences, George Mason University, Fairfax, Virginia, USA, [2]School of Earth and Space Exploration, Arizona State University, Tempe, Arizona, USA, [3]Department of Earth, Atmospheric and Planetary Sciences, Massachusetts Institute of Technology, Cambridge, Massachusetts, USA, [4]NASA Goddard Space Flight Center, Greenbelt, Maryland, USA, [5]Astrogeology Science Center, U.S. Geological Survey, Flagstaff, Arizona, USA, [6]Malin Space Science Systems, San Diego, California, USA, [7]Department of Geological and Planetary Sciences, California Institute of Technology, Pasadena, California, USA, [8]Geology Faculty, Department of Geocryology, Moscow State University, Moscow, Russia, [9]Department of Planetary Sciences and Remote Sensing, Freie University, Berlin, Germany

Abstract The small crater Airy-0 was selected from Mariner 9 images to be the reference for the Mars prime meridian. Initial analyses in the year 2000 tied Viking Orbiter and Mars Orbiter Camera images of Airy-0 to the evolving Mars Orbiter Laser Altimeter global digital terrain model to update the location of Airy-0. Based upon this tie and radiometric tracking of landers/rovers from Earth, new expressions for the Mars spin axis direction, spin rate, and prime meridian epoch value were produced to define the orientation of the Martian surface in inertial space over time. Since the Mars Global Surveyor mission and Mars Orbiter Laser Altimeter global digital terrain model were completed some time ago, a more exhaustive study has been performed to determine the accuracy of the Airy-0 location and orientation of Mars at the standard epoch. Thermal Emission Imaging System (THEMIS) IR image cubes of the Airy and Gale crater regions were tied to the global terrain grid using precision stereo photogrammetric image processing techniques. The Airy-0 location was determined to be about 0.001° east of its predicted location using the currently defined International Astronomical Union (IAU) prime meridian location. Information on this new location and how it was derived will be provided to the NASA Mars Exploration Program Geodesy and Cartography Working Group for their assessment. This NASA group will make a recommendation to the IAU Working Group on Cartographic Coordinates and Rotational Elements to update the expression for the Mars spin axis direction, spin rate, and prime meridian location.

1. Introduction

Knowledge of the Mars orientation in inertial space is required when targeting landers to specific locations, observing its surface from Earth and spacecraft, for tracking landers on the surface of Mars from orbiters and directly from Earth, for determining the gravity field from orbiting spacecraft, etc. The orientation is defined by the Mars spin axis direction, the location of the prime meridian, and the spin rate to propagate the orientation over time. The Mars orientation originally had been determined from Earth-based telescopic observation where the large crater Sinus Meridiani was adopted as the prime meridian reference. The location of Mars surface features in inertial space when propagating ahead in time had an accuracy at the tens of kilometers level due to errors in spin axis direction and spin rate. After the Mariner 6 and 7 flybys and Mariner 9 orbiter explorations, the knowledge of the orientation of Mars in inertial space was improved to the 10 km level. *de Vaucouleurs et al.* [1973] refined the prime meridian reference by using Mariner 9 images to fix it to the small crater Airy-0 within the large crater Airy.

The spin axis direction and spin rate continued to be improved by the Earth-based tracking of the Viking and Mars Pathfinder landers. Improvements to the location of the crater Airy-0 came after the orbiting Mars Global Surveyor (MGS) [*Albee and Arvidson*, 1991] started producing a global digital terrain model (DTM) from its Mars Orbiter Laser Altimeter (MOLA) [*Smith et al.*, 2001] in the late 1997. By the end of 2001, MOLA had amassed over 600 million altimeter points, distributed globally with an average spacing of 300 m in

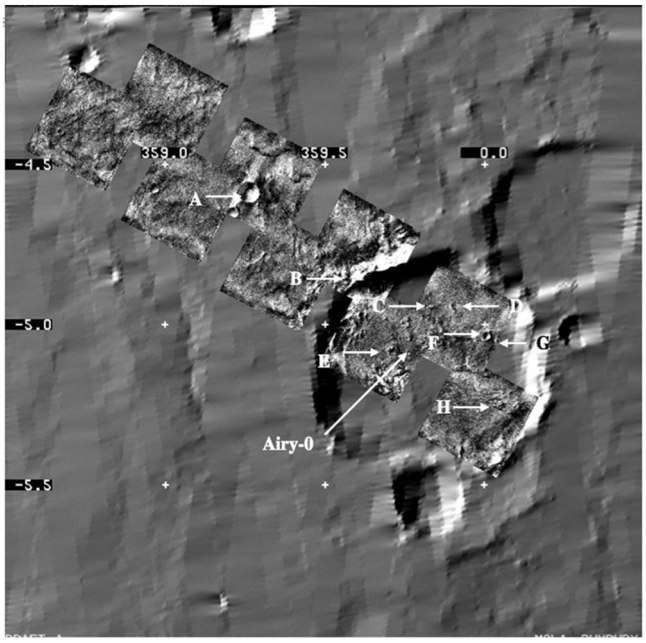

Figure 1. In 2001, the Airy-0 location was determined by registering nine Viking Orbiter images to an early MOLA DIM with features A–H being MOLA control points.

latitude and 2 km spacing in longitude at Mars equator. With each MGS orbit crossing over thousands of other orbits and since there were thousands of orbits, millions of MOLA crossover points were available for detailed processing. The differences between all individual observed and predicted altimetry points where orbits crossed are now at the meter level, obtained by constraining the MGS spacecraft orbits and pointing to fit mill ions of orbit crossover altimetry points together with a precision gravity field [*Neumann et al.*, 2001]. However, tying imaging data to the individual MOLA points is limited at the 100 m level due to the larger spacing of the MOLA points in latitude and longitude. The MOLA global DTM was the most significant development for precision Mars cartography since the beginning of Mars exploration. A detailed history of the Mars prime meridian is given in *Archinal and Caplinger* [2002].

In 2000, the International Astronomical Union (IAU) Working Group on Cartographic Coordinates and Rotational Elements (WGCCRE) was preparing its publication that would include the spin axis, spin rate, and prime meridian expressions for Mars. Even though the MOLA data coverage was far from complete and the precision cartographic processing had only begun, the MOLA data set was sufficient to register a Viking Orbiter-controlled photomosaic to a MOLA-derived digital image model (DIM) by one of the authors (Duxbury) in 2001 (Figure 1). Also, a single Mars Orbiter Camera [*Malin et al.*, 1992] image was registered to a single MOLA ground track by two of the authors (Caplinger and Neumann) in 2001. These two efforts gave solutions of the areocentric coordinates of Airy-0 that agreed within a few hundred meters. Those were averaged to produce the location of Airy-0 relative to the MOLA grid that was adopted within the NASA Mars Exploration Program Office by its Geodesy and Cartography Working Group (MGCWG) [*Duxbury et al.*, 2002].

Airy-0 was found to be 0.25° or 15 km from the IAU reference position. The fundamental epoch angle (W_0) of the IAU prime meridian expression was adjusted as were the longitudes of all MOLA points, so when images of Airy-0 were registered to MOLA, Airy-0 would have a computed longitude of 0°. The spin axis direction, spin rate, and prime meridian expressions based upon this Airy-0 location and the spin axis/rate work by *Yuan et al.* [2001] are referred to as the "IAU 2000 pole and prime meridian of Mars" [*Seidelmann et al.*, 2002].

Since this WGCCRE publication, no work had been performed to improve the location of Airy-0 until the MGCWG recently initiated studies of the Mars orientation to support a new IAU WGCCRE publication to update the Mars orientation expressions. Based upon this revived interest, new results of the Airy-0 location are presented in this article. Stereo photogrammetric data processing was used to register multispectral infrared image cubes to MOLA and High Resolution Stereo Camera (HRSC) [*Neukum et al.*, 2009] DTMs. The 2001 Mars Odyssey (ODY) [*Saunders et al.*, 2004] Thermal Emission Imaging System (THEMIS) IR [*Christensen et al.*, 2004] image cubes of the Airy crater and Gale crater comprised the image data set. The precision global MOLA DTM, the local HRSC DTM, and THEMIS IR image cubes did not exist in 2001; therefore, there is significant independence of the results presented here to the earlier 2001 results.

The spatial resolution of the THEMIS image cubes is 100 m/pixel. MOLA DTMs surrounding Airy and Gale craters were constructed from all of the individual final/corrected MOLA ground tracks [*Neumann et al.*, 2001] within these areas and illuminated under similar conditions as each of the THEMIS IR image cubes to produce DIMs at 230 m/pixel. Additionally, a DTM and DIM of Gale crater were produced by the German Space Center (DLR) [*Gwinner et al.*, 2010] that were derived by registering HRSC stereo images to MOLA with

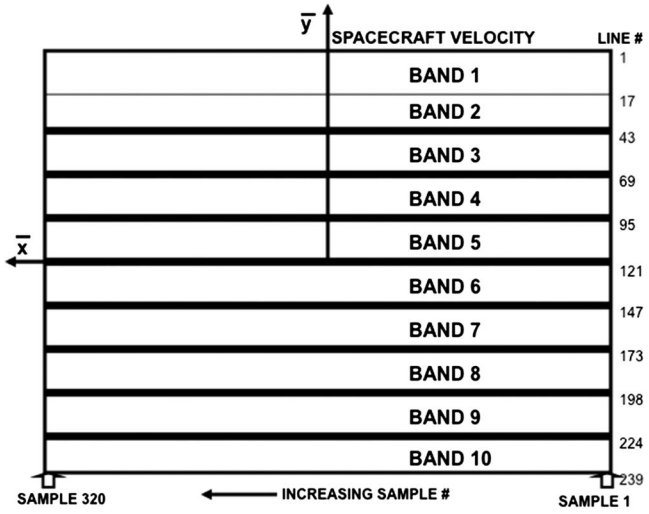

Figure 2. THEMIS IR microbolometer area array layout with 10 spectral bands looking down on the array.

a spatial resolution of 50 m/pixel (http://europlanet.dlr.de/node/index.php?id=380GaleDTM). The Airy crater data reduction gave the direct location of Airy-0, while the Gale crater data reduction gave an independent verification of the THEMIS IR geometric parameter values versus those derived with the Airy-0 location and the stability of the THEMIS IR parameter values over time and over the Martian surface.

By-products of this analysis included precision 10-band THEMIS IR-controlled photomosaics of the Airy and Gale crater regions with thousands of precision control and tie points. The controlled photomosaic of Gale crater was used by the MGCWG to provide an independent validation of the map products used by the Mars Surface Laboratory (MSL) [*Grotzinger et al.*, 2012] flight operations team to plan and target its successful landing. Precision THEMIS IR geometric and pointing calibrations, archived as NAIF SPICE [*Acton*, 1996; *Semenov et al.*, 2005] Instrument (IK) and Frames (FK) kernels, were produced as part of the stereo photogrammetric reduction. These kernels were used in producing the THEMIS IR 100 m/pixel, 10-band global Mars digital image mosaic (MDIM) [*Edwards et al.*, 2011]. Additionally, the precision and noise characteristics of the reconstructed ODY spacecraft attitude were determined over an 8 year time period.

The following sections describe the cartographic mapping properties of THEMIS IR, how local DTM control point and THEMIS tie point networks were established in the Airy and Gale crater regions, how the THEMIS IR image cubes were measured to produce the tens of thousands of linear equations used in the stereo photogrammetric reduction process, how the THEMIS IR images were registered to the MOLA/HRSC reference surfaces for absolute control, how the observations were validated and weighted, the results of the data reduction in determining the location of Airy-0, the THEMIS IR geometric and alignment parameter values, the precision/noise characteristics of the observations, the control and tie point networks, and the spacecraft attitude data over the two crater sites and over 8 years of time.

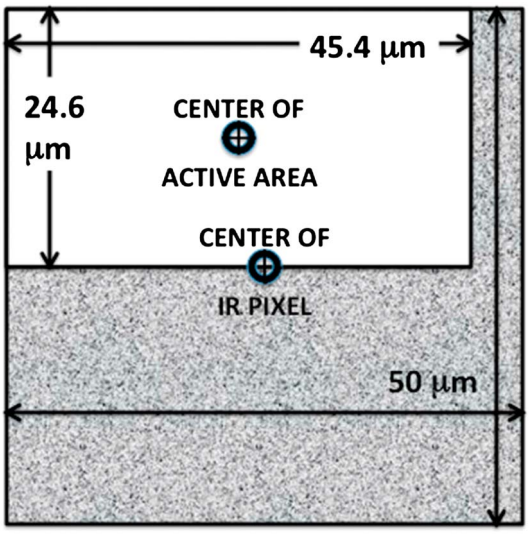

Figure 3. THEMIS IR active pixel area.

2. Cartographic Mapping Properties of THEMIS IR

THEMIS produces both multispectral infrared (IR) push broom and multispectral visual (VIS) area array images. To date, these images have been mostly taken along the spacecraft ground track, but recently, some images have been taken off nadir. The THEMIS IR uses a 320 × 240 pixel microbolometer area array with different narrowband spectral filters covering 10 sections of the detector (Figure 2). Each filter covers 16 lines that are read out at a rate designed to match the ground track speed from the near-circular and near-polar ODY orbit. Line summing of the 16 lines within each spectral band, using time delay integration, produces one effective image line for each band to increase the signal-to-noise ratio. Therefore, in normal IR imaging mode, 10 equivalent lines,

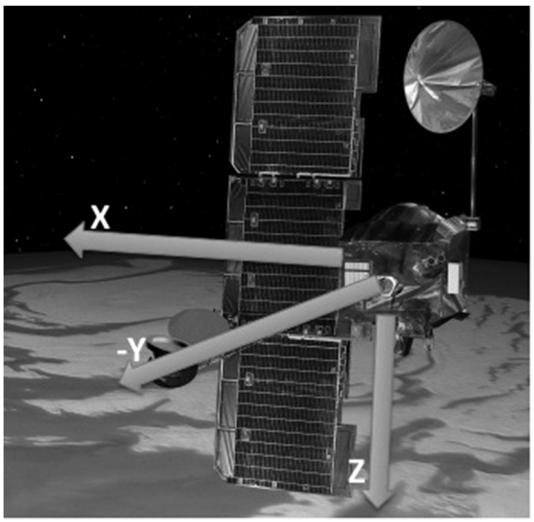

Figure 4. The NASA Mars Odyssey spacecraft-fixed $\bar{\mathbf{X}}\bar{\mathbf{Y}}\bar{\mathbf{Z}}$ coordinate system.

covering narrow IR spectral bands, form the push broom, multispectral image cubes.

A THEMIS IR pixel within the microbolometer area array is 50×50 μm^2, but only a 45.4×24.6 μm^2 area is active (Figure 3) to image Mars, thus limiting image metric measurement residuals to the few tens of a pixel level. This occurs because each of the 16 pixels summed to produce one effective pixel per spectral band and the effective pixels in the other nine different bands have each seen a slightly different view of the surface due to spacecraft orbital, attitude, and Mars rotational motion during image construction. An automated digital image matching/correlation technique cannot achieve greater accuracy because the pixels will not match exactly, even if they have the same spectral band pass.

Each of the 10 IR bands share optical distortion and spacecraft mounting alignment/pointing parameters but have slightly different values for time tag, pointing, spacecraft position, and focal length.

In order to relate individual THEMIS IR image pixels to Mars-fixed surface coordinates, multiple reference systems are used that include the following.

2.1. Mars-Fixed System

The Mars Mean Equator and prime meridian of-date reference system has axes $\bar{\mathbf{X}}_\mathbf{m}\bar{\mathbf{Y}}_\mathbf{m}\bar{\mathbf{Z}}_\mathbf{m}$ where $\bar{\mathbf{X}}_\mathbf{m}$ and $\bar{\mathbf{Y}}_\mathbf{m}$ define the Mars equator and $\bar{\mathbf{Z}}_m$ defines the Mars pole (spin axis): (1) $\bar{\mathbf{X}}_m$ is in the of-date Mars equator and along the prime meridian tied to the crater Airy-0; (2) $\bar{\mathbf{Z}}_m$ is along the of-date Mars north pole; and (3) $\bar{\mathbf{Y}}_m$ is in the of-date Mars equator, completing the orthogonal, right-handed system.

The orientation of these axes in inertial space at any Barycentric Dynamical Time, TDB, referred to as "of-date," is recommended by the IAU WGCCRE [*Archinal et al.*, 2011] based on *Duxbury et al.* [2002] and are included in the NAIF SPICE Planetary Constants kernel ftp://naif.jpl.nasa.gov/pub/naif/M01/kernels/pck/pck00010.tpc.

A Mars-centered and fixed surface position vector $\bar{\mathbf{u}}$ having areocentric coordinates of latitude, ϕ positive north, longitude, λ positive east, and radius, u in kilometers, is given by

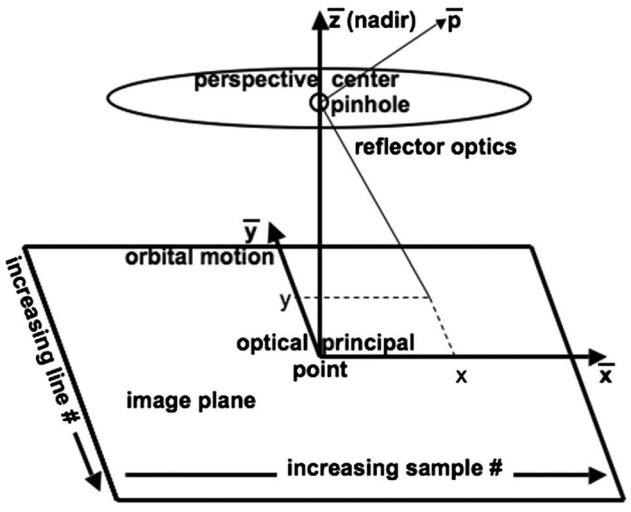

Figure 5. THEMIS IR microbolometer area array image plane coordinates looking down on the array.

$$\bar{\mathbf{u}} = u \begin{bmatrix} \cos\phi\ \cos\lambda \\ \cos\phi\ \sin\lambda \\ \sin\phi \end{bmatrix} = \begin{bmatrix} u_x \\ u_y \\ u_z \end{bmatrix} \text{ (km)} \quad (1)$$

where u_x, u_y, and u_z are the position components of $\bar{\mathbf{u}}$ along the Mars-fixed axes $\bar{\mathbf{X}}_\mathbf{m}\bar{\mathbf{Y}}_\mathbf{m}\bar{\mathbf{Z}}_\mathbf{m}$.

The Mars-centered and fixed position vector $\bar{\mathbf{u}}$ is translated to the spacecraft-centered and Mars-fixed position vector $\bar{\mathbf{v}}$ using

$$\bar{\mathbf{v}} = \bar{\mathbf{u}} - \bar{\mathbf{w}} \text{ (km)} \quad (2)$$

where $\bar{\mathbf{w}}$ is the Mars-centered and fixed spacecraft position vector at TDB obtained from a NAIF SPICE spacecraft ephemeris kernel ftp://naif.jpl.nasa.gov/pub/naif/M01/kernels/spk/*.bsp.

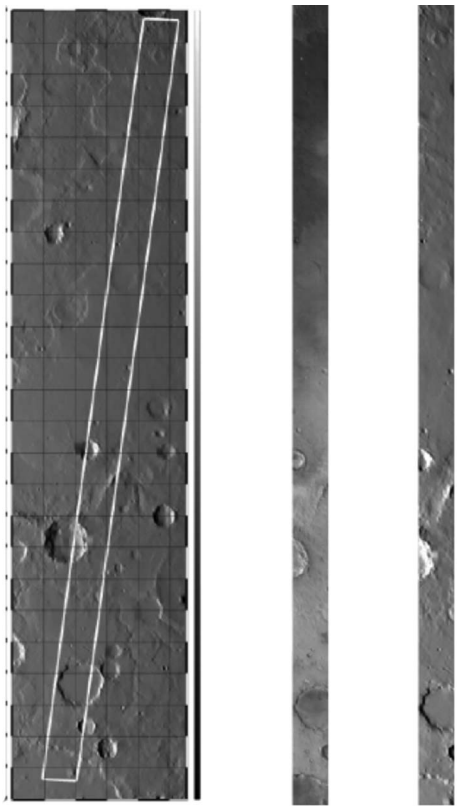

Figure 6. Simulated THEMIS IR image in Marwth by illuminating a MOLA-derived DTM to produce a DIM under the same lighting conditions as the THEMIS IR cube. (left) MOLA DIM, (middle) IR band 5 image, and (right) simulated IR image from MOLA DIM.

The .bsp files having "mgs095j" in the file name have absolute position accuracies at the meter level [*Konopliv et al.*, 2011] and were used in this analysis. At this level of accuracy, the ODY positions at the times of the image cubes were not estimated but were held as fixed parameters.

2.2. The 2001 Mars Odyssey Spacecraft System

The ODY spacecraft-fixed coordinate system has axes $\bar{\mathbf{X}}\bar{\mathbf{Y}}\bar{\mathbf{Z}}$ (Figure 4) where during normal orbital operations, $\bar{\mathbf{Z}}$ is nadir pointed toward Mars; $\bar{\mathbf{X}}$ is canted 17° from the orbit plane, orthogonal to $\bar{\mathbf{Z}}$; and $\bar{\mathbf{Y}}$ completes the orthogonal, right-handed system.

The 3 × 3 unitless transformation matrix **C** defines the orientation of the Odyssey spacecraft in Mars-fixed coordinates and is reconstructed from telemetered quaternions based upon star camera and inertial measurement unit observations. The **C** matrix allows one to transform from the of-date Mars body-fixed system to the Odyssey spacecraft-fixed coordinate system using:

$$\begin{bmatrix} \bar{\mathbf{X}} \\ \bar{\mathbf{Y}} \\ \bar{\mathbf{Z}} \end{bmatrix} = \mathbf{C} \begin{bmatrix} \bar{\mathbf{X}}_{\mathbf{m}} \\ \bar{\mathbf{Y}}_{\mathbf{m}} \\ \bar{\mathbf{Z}}_{\mathbf{m}} \end{bmatrix} \tag{3}$$

where **C** is obtained from the 2001 Mars Odyssey NAIF SPICE archive ftp://naif.jpl.nasa.gov/pub/naif/M01/kernels/ck/*.bc.

Given a **C** kernel [*Acton*, 1996], the spacecraft-centered and Mars-fixed position vector $\bar{\mathbf{v}}$ is transformed to a spacecraft centered and fixed position vector $\bar{\mathbf{r}}$ by using

$$\bar{\mathbf{r}} = \mathbf{C}\,\bar{\mathbf{v}} \ \text{(km)} \tag{4}$$

For 2001 Mars Odyssey, the noise on the **C** kernels was found to be about 0.01° (3σ).

2.3. THEMIS IR-Fixed System

The THEMIS IR base/optics (**TO**) are hard mounted to the spacecraft. The alignment of this base system relative to the ODY spacecraft axes was determined prelaunch and will be held fixed for this analyses. The transformation $\mathbf{T}_{\mathbf{TO}}^{\mathbf{ODY}}$ from the ODY-fixed $\bar{\mathbf{X}}\bar{\mathbf{Y}}\bar{\mathbf{Z}}$ to the THEMIS base/optics system **TO** is defined by

$$\mathbf{T}_{\mathbf{TO}}^{\mathbf{ODY}} = \left[-0.02378^{o}\right]_1 \left[-0.06119^{\circ}\right]_2 \left[-16.91498^{\circ}\right]_3 \tag{5}$$

where the $\approx -17°$ rotation about the third axis removes the spacecraft cant angle to align the THEMIS IR lines normal to the orbit plane. The form $[\theta]_i$ for $i = 1$, 2, or 3 represents a unitless 3 × 3 rotation matrix given by

$$[\theta]_1 = \begin{bmatrix} 1 & 0 & 0 \\ 0 & \cos\theta & \sin\theta \\ 0 & -\sin\theta & \cos\theta \end{bmatrix},$$

$$[\theta]_2 = \begin{bmatrix} \cos\theta & 0 & -\sin\theta \\ 0 & 1 & 0 \\ \sin\theta & 0 & \cos\theta \end{bmatrix},$$

and

$$[\theta]_3 = \begin{bmatrix} \cos\theta & \sin\theta & 0 \\ -\sin\theta & \cos\theta & 0 \\ 0 & 0 & 1 \end{bmatrix}. \tag{6}$$

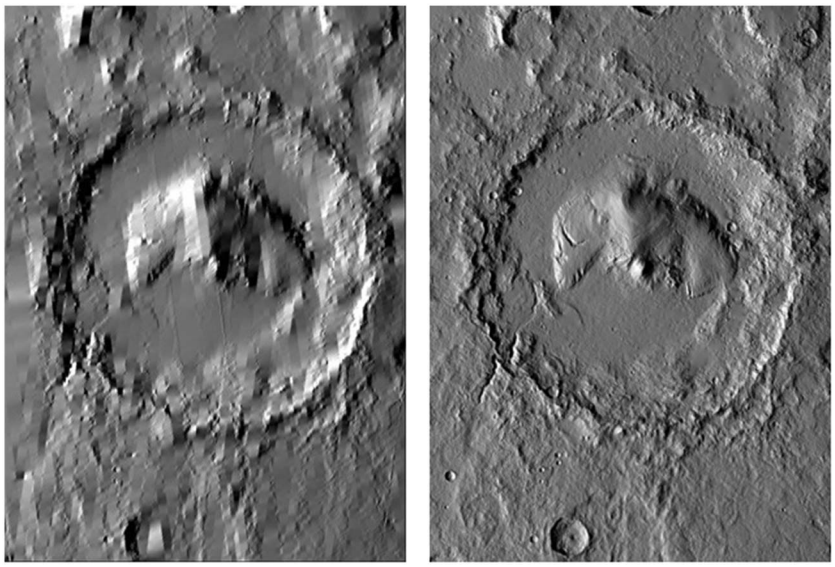

Figure 7. (left) MOLA- and (right) HRSC-derived DIMs.

From this base/optics system, one can then transform to the THEMIS IR-fixed microbolometer area array coordinate system that has axes $\bar{\mathbf{x}}\bar{\mathbf{y}}\bar{\mathbf{z}}$ (Figures 2 and 5) where $\bar{\mathbf{x}}$ is in the direction of increasing IR sample numbers and normal to the orbit plane; $\bar{\mathbf{z}}$ is along the nadir direction during nadir operations; and $\bar{\mathbf{y}}$ completes the orthogonal, right-handed system, is along the decreasing line direction, and is in the general direction of the spacecraft velocity vector.

The following 3 × 3 unitless transformation matrix $\mathbf{T}_{\mathbf{IR}}^{\mathbf{TO}}$ from THEMIS base/optics to THEMIS IR fixed $\bar{\mathbf{x}}\bar{\mathbf{y}}\bar{\mathbf{z}}$ coordinates is expressed as

$$\mathbf{T}_{\mathbf{IR}}^{\mathbf{TO}} = \left[\theta_w\right]_3 \left[\theta_y\right]_2 \left[\theta_z\right]_3 \tag{7}$$

From ground calibrations, $\theta_z = 0.0°$, $\theta_y = 90°$, and $\theta_w = 0.672°$.

As previously mentioned, the angles in equation (5) will be held fixed but the angles in equation (7) will be solved for in the stereo photogrammetric reduction process where there will be three estimated angles for each 10-band IR image cube. The averages of these three angles over all IR cubes will be referred to as the fixed mounting alignment angles, and the differences between the fixed biases and the individual values for each cube will be used to asses the spacecraft attitude pointing accuracy and stability.

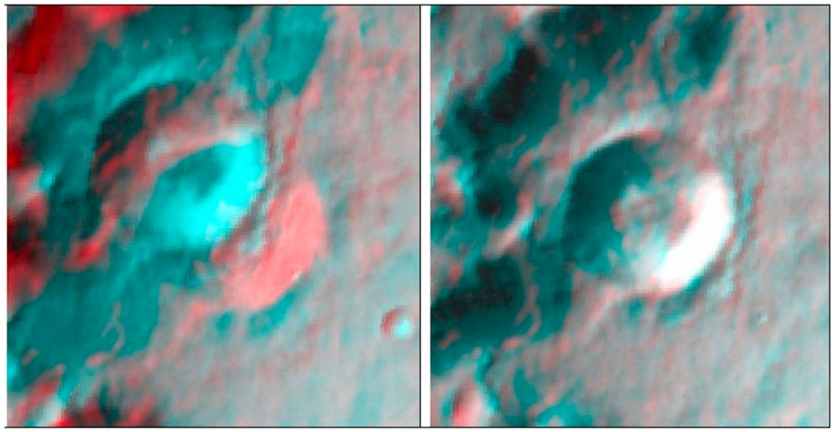

Figure 8. An IR image was registered to the HRSC DIM of the same feature to measure control point locations. Image misregistration produces red/blue-green ghost images as seen on the left.

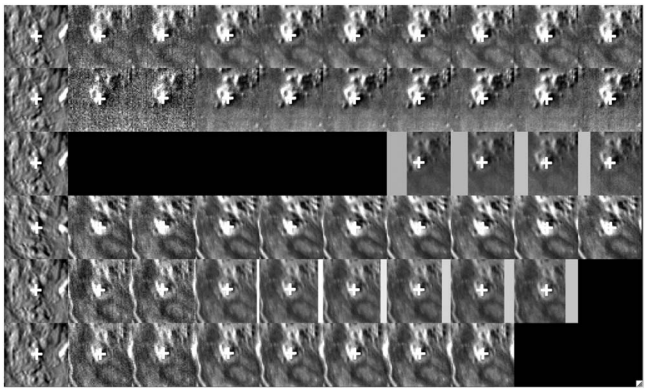

Figure 9. Measured and predicted image locations were displayed as plus and cross overlays, respectively, to validate measurements in all bands and all cubes. Usually, the measured and predicted overlays were on top of each other so only the plus was seen as is the case here where the stereo reduction process was completed and all bad image location measurements were corrected or removed. These residuals, the difference between the measured and predicted image locations, verified that the measurement accuracy was at a subpixel level. Note that subpixel measurement accuracy was achieved even with the significantly different appearance of the features due to the thermal properties in the different spectral bands and different viewing/lighting conditions.

Equations (5) and (7) can be concatenated to give the transformation $\mathbf{T}_{\mathbf{IR}}^{\mathbf{ODY}}$ from ODY-fixed to THEMIS IR-fixed coordinates by

$$\mathbf{T}_{\mathbf{IR}}^{\mathbf{ODY}} = \mathbf{T}_{\mathbf{IR}}^{\mathbf{TO}}\,\mathbf{T}_{\mathbf{TO}}^{\mathbf{ODY}} \tag{8}$$

The spacecraft centered and fixed position vector $\bar{\mathbf{r}}$ in equation (4) can then be transformed to a THEMIS centered and fixed position vector $\bar{\mathbf{p}}$ by

$$\bar{\mathbf{p}} = \mathbf{T}_{\mathbf{IR}}^{\mathbf{ODY}}\,\bar{\mathbf{r}} = \begin{bmatrix} p_x \\ p_y \\ p_z \end{bmatrix} \quad \text{(km)} \tag{9}$$

where p_x, p_y, and p_z are the components of position vector $\bar{\mathbf{p}}$ in THEMIS IR-centered and fixed $\bar{\mathbf{x}}\bar{\mathbf{y}}\bar{\mathbf{z}}$ coordinates.

2.4. THEMIS IR Focal Plane/ Image Coordinates

There are multiple methods to map from the THEMIS-fixed position vector $\bar{\mathbf{p}}$ through the optics to the focal plane and then to THEMIS IR image coordinates. In mapping through the optics to the image plane, a square shape in object space becomes a "keystone" shape in the image. THEMIS uses a beam splitter to focus some light onto the IR detector with the rest of the light onto the VIS detector. One explanation for the keystone effect is that the beam splitter is not exactly aligned 45° going to the IR detector. The net effect, from whatever the cause, is that each of the 10 bands has a different scale along the 320 samples within a line. The first model used in this analysis to map from $\bar{\mathbf{p}}$ to image coordinates will give each of the 10 bands its own focal length along the 320 samples.

Selecting a scale across the 10 bands also has its problems. Since each band has its own focal length along each line, no single focal length can be used to represent the scale across all 10 lines and obtain subpixel model accuracy. However, a single scale in the line direction was implemented in the first model, and then a bias was added to each band locations to account for the differences between the single line scale and the actual band locations. This model provides parameters that are easily visualized and gives quick insight into the THEMIS IR geometric properties.

The nominal image plane x, y mm coordinates (Figures 2 and 5) on the THEMIS IR area array detector, associated with $\bar{\mathbf{p}}$, are computed using the colinear equation of photogrammetry [*Thompson*, 1966] where the camera optics are modeled as a pinhole

$$\begin{bmatrix} x \\ y \end{bmatrix} = \frac{1}{p_z}\begin{bmatrix} f_i p_x \\ f\,p_y \end{bmatrix} \quad \text{(nominal, mm)} \tag{10}$$

where f_i is the THEMIS IR effective focal length along the sample direction $\bar{\mathbf{x}}$ for each of the IR bands (i=1,...,10) and f is an average focal length along the line direction $\bar{\mathbf{y}}$, across all of the IR bands.

If the optics produce radial distortion, the actual image plane coordinates x' and y' are shifted relative to the nominal x, y mm coordinates and are computed from

$$\begin{bmatrix} x' \\ y' \end{bmatrix} = \begin{bmatrix} x \\ y \end{bmatrix} + r^2\begin{bmatrix} x \\ y \end{bmatrix}\alpha_1 + r^4\begin{bmatrix} x \\ y \end{bmatrix}\alpha_2 \quad \text{(distorted, mm)} \tag{11}$$

where

$$r^2 = x^2 + y^2 \quad \text{mm}^2 \tag{12}$$

and where α_1 and α_2 are the coefficients of radial optical distortion. An optical distortion term proportional to r would not be distinguishable from a change in focal length and is not included in the model. Equation (11) assumes that the optical principal point is at the center of the THEMIS IR area array detector, an approximation that this analysis found was sufficient to maintain subpixel model accuracy.

The predicted THEMIS IR sample s and line l image coordinates, associated with the position vector $\bar{\mathbf{p}}$, are computed from

$$\begin{bmatrix} s \\ l \end{bmatrix} = \begin{bmatrix} s_0 \\ l_0 \end{bmatrix} + K \begin{bmatrix} x' \\ -y' \end{bmatrix} + \begin{bmatrix} 0 \\ b_i \end{bmatrix} \quad \text{(raw image coordinates)} \tag{13}$$

For THEMIS IR, $s_0 = 160.5$, $l_0 = 120.5$, the IR area array center coordinates, and $K = 20.000$ pixels/mm since a THEMIS IR pixel is 0.050 mm across. These three CCD parameter values are fixed and are not estimated. The minus sign is needed in equation (13) for the y' coordinate since $\bar{\mathbf{y}}$ is in the direction of decreasing line number. The b_i terms absorb errors in approximating the scale in the line direction $\bar{\mathbf{y}}$ with a single focal length f and are a fraction of an IR pixel.

Because of systematic residual errors when using the first model, a second model was additionally evaluated to map from position vector $\bar{\mathbf{p}}$ to THEMIS IR image coordinates s and l. Given the THEMIS IR centered and fixed position vector $\bar{\mathbf{p}}$ to a surface feature, one can compute the IR focal plane coordinates x and y

$$\begin{bmatrix} x \\ y \end{bmatrix} = \frac{f_k}{p_z} \begin{bmatrix} p_x \\ p_y \end{bmatrix} \quad \text{(nominal, mm)} \tag{14}$$

where f_k is the average focal length across the entire IR focal plane. THEMIS IR image coordinates s and l are then computed directly from

$$\begin{bmatrix} s \\ l \end{bmatrix} = \begin{bmatrix} s_0 \\ l_0 \end{bmatrix} + K \begin{bmatrix} K_{11} & K_{12} & K_{13} & K_{14} & K_{15} \\ K_{21} & K_{22} & K_{23} & K_{24} & K_{25} \end{bmatrix} \begin{bmatrix} x \\ y \\ xy \\ x^2 \\ y^2 \end{bmatrix} \tag{15}$$

For the case of no optical or keystone distortions, $K_{11} = 1$, $K_{22} = -1$, the rest of the K terms have values of zero, and K, s_0, and l_0 have the same values as in equation (13). The values of f_k and K_{ij} are estimated parameters.

As mentioned previously, the IR area array detector is divided into 10 areas under different narrowband IR filters where 16 lines within these bands are summed to produce better signals, yielding one equivalent line observation per band (Figure 2). The center line number of each band is adopted here as the observed line coordinate of any feature (e.g., a control point) within that band. Therefore, the observed image coordinate of a feature can have a sample value s ranging between 1 and 320, but the observed line coordinate l in equations (13) and (15) is fixed for each of the 10 IR bands that have the following values:

$$\begin{aligned} l_1 &= 8.5 \text{ for IR band \#1} \\ l_2 &= 24.5 \text{ for IR band \#2} \\ l_3 &= 50.5 \text{ for IR band \#3} \\ l_4 &= 76.5 \text{ for IR band \#4} \\ l_5 &= 102.5 \text{ for IR band \#5} \\ l_6 &= 128.5 \text{ for IR band \#6} \\ l_7 &= 154.5 \text{ for IR band \#7} \\ l_8 &= 180.5 \text{ for IR band \#8} \\ l_9 &= 205.5 \text{ for IR band \#9} \\ l_{10} &= 231.5 \text{ for IR band \#10} \end{aligned} \tag{16}$$

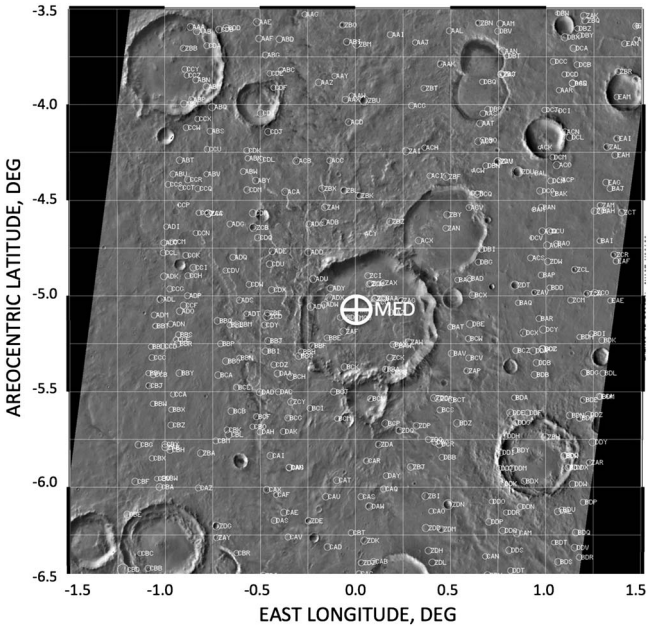

Figure 10. A seamless controlled THEMIS IR photomosaic of the Martian Airy crater area showing all control and tie points. The more dense population of control and tie points in the north-south direction are in areas of IR cube overlap. Tie point MED near the center and identified by the circled plus is Airy-0.

3. Time Tag

When one is measuring an IR image cube file (.QUB), one measures the record number L in the file of a feature location. The value of L is not used as the line observation associated with equation (13) or (15). The line observation is always one of the 10 values of l_i listed in equation (16). The value of L is used to determine the time tag of the s_i, l_i observation.

The readout rate within the IR area array is constant and is not affected by $f_i, f, b_i, \alpha_1, \alpha_2, f_k, K_{ij}$ and is $\sim$ 30 lines/s. The start time of an IR image, defined in the QUB image file label record, gives the time of the first line in the entire area array detector. The time tag of any sample s in one of the 10 equivalent lines must include the time needed to read out the detector down to l_i, i=1,...,10.

Given an observed s_i, l_i image location of a control point in band $i, i = 1, ..., 10$ at QUB image record L, the timing offset Δt from the start time given in the QUB label record for the observed image coordinates is computed from

$$\Delta t = \frac{l_i + L - 1}{\text{RATE}} \text{ s} \tag{17}$$

For $L = 1$ of band $i = 1$, the time offset for this band is $\sim$ 0.55 s from the image start time defined in the QUB label record.

The start time of an image cube could have an uncertainty of up to four IR image lines. An error in the cube start time and an error in angle θ_y are similar, only effecting the line direction, and cannot be separated in the stereo reduction process. Therefore, an error in Δt for each IR image cube is not estimated, so its effect will be included in the estimated value for θ_y.

An example of using equations (1)–(5) is shown in Figure 6. A MOLA DTM in the Marwth region of Mars was illuminated under the same lighting conditions as a THEMIS IR cube (middle) to produce the map gridded DIM (left). Going backward through equations (1)–(15) and using the associated NAIF SPICE kernels, band 5 of the IR cube was simulated (right). One could then vary the modeled surface properties in an attempt to bring the simulated image into agreement with the actual image brightness to infer surface scattering/thermal properties (not included in the scope of this analyses). In producing this simulated THEMIS IR image that was registered to the MOLA DIM, a readout rate of 30.0147 lines/s was determined, consistent with the prelaunch calibrated value of 30.0477 lines/s. Over a typical 15 s THEMIS IR image, the difference in readout rates maps to less than 0.5 lines. This in-flight determined value was held constant in the stereo photogrammetric reduction processing across all THEMIS IR cubes.

4. Stereo Photogrammetric Linear Equations

Equations (1)–(15) allow one to map a location on the surface of Mars to a sample/line image location in any band of a THEMIS IR cube given the START_TIME from the image label record and the associated NAIF SPICE

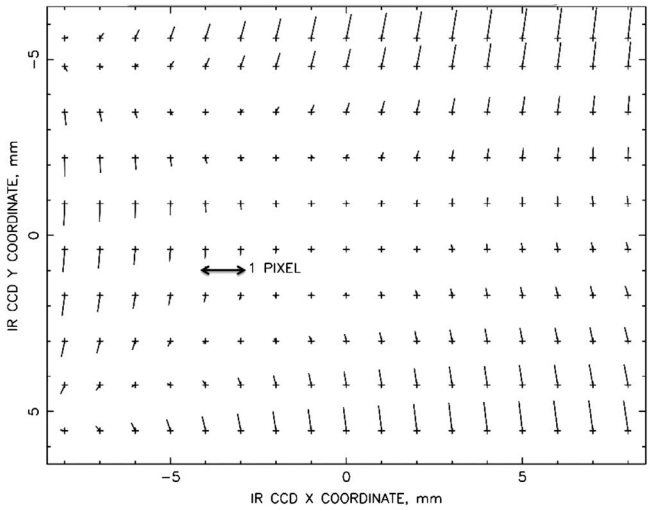

Figure 11. The difference is shown between the two THEMIS IR geometric models. The systematic differences between these two models are due to the lack of freedom in the model 1 parameters that model 2 provides.

kernels. One can also use these equations to go backward from image location s, l to Mars-fixed surface coordinates, given a local Mars radius or digital terrain model of the area imaged.

For the stereo photogrammetric analyses of THEMIS IR cubes performed here, the first-order partial derivatives of s, l with respect to $f_i, f, b_i, \alpha_1, \alpha_2, f_k, K_{ij}, \theta_z, \theta_y, \theta_w, \phi, \lambda, u$ are used to construct linear equations where the measured image locations of surface features in IR cubes are used as observables in a square root, weighted least squares estimation process [*Bierman*, 1977] to determine the THEMIS IR geometric, alignment, and pointing parameters and the control/tie point locations on the surface of Mars, including Airy-0.

MOLA DTMs and DIMs and HRSC-derived DTMs and DIMs (precisely tied to MOLA) provide "absolute control" in registering image cubes to the Mars reference surface. The term absolute control is used to reflect that the millions of MOLA points have been tied together globally at the meter level but is limited by their 300 m spacing in latitude between points and a few kilometer spacing in orbital longitude at Mars equator. Therefore, the DTMs and DIMs provide similar absolute information as a star catalog does for astrometric reductions. Finally, when all camera parameters and surface feature locations are determined, one can produce precision (subpixel accuracy) multiband, controlled photomosaics using equations (1)–(15) by running through a range of ϕ and λ at a fixed spatial resolution using a standard map projection and populating the mosaic with the appropriate IR image pixel brightness values. The MOLA DTM was used as the reference surface to produce the Airy crater-controlled photomosaic, and the HRSC DTM was used as the reference surface to produce the Gale crater-controlled photomosaic. The map-projected THEMIS IR image cubes and the bands within each cube were registered seamlessly to better than 0.3 pixels (1σ), the tie point measurement accuracy.

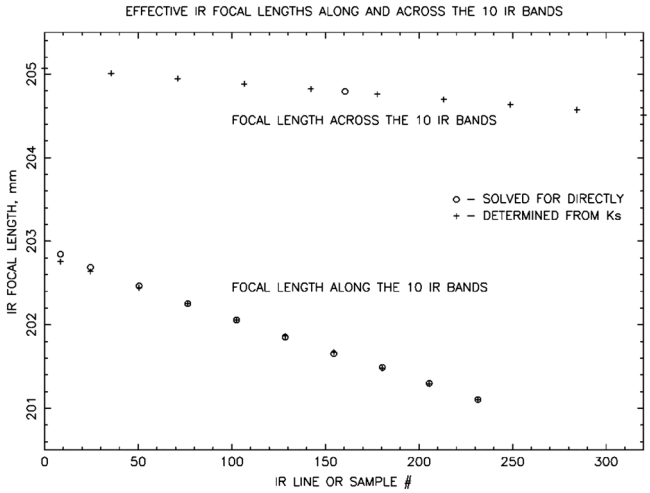

Figure 12. The solved for and derived THEMIS IR equivalent focal lengths are displayed as a function of band and CCD location. The focal lengths indicated by plus were derived from the K term values using equations (20) and (21).

5. THEMIS IR Control and Tie Point Measurements

Photomosaics were produced in sinusoidal map projections having spatial resolutions of 100 m/pixel for both Airy and Gale craters using THEMIS IR band 5 images, a priori THEMIS IR parameter values, the associated SPICE kernels, and equations (1)–(15). Misalignment in the areas of image cube overlap was obvious because of errors in the image projections due to errors in the THEMIS IR parameter values, random noise in the THEMIS pointing (**C** kernel), and errors in start times of the image cubes. A low-resolution version of a mosaic

was displayed on a large cinema monitor that allowed the user to poke on any position within the mosaic and display all THEMIS IR cubes/bands that covered the point. Because of the large number of overlapping cubes being measured, up to six THEMIS IR cubes with all 10 bands within each cube could cover a point.

To easily and quickly transform between photomosaic ϕ, λ space and THEMIS IR cube s, l space, equations (1)–(15) were evaluated 300 times, evenly spaced between samples 1 and 320 and between all of the IR image lines that were within the map projection limits for each band of all cubes. These sets of 300 ϕ, λ, s, l groups for each band of all cubes were used to determine the coefficients in the following approximate transformations, assuming a constant Mars radius within the photomosaic:

$$\begin{bmatrix} s \\ l \end{bmatrix} = \begin{bmatrix} s_0 \\ l_0 \end{bmatrix} + \begin{bmatrix} s_1 & s_2 & s_3 & s_4 \\ l_1 & l_2 & l_3 & l_4 \end{bmatrix} \begin{bmatrix} \lambda \\ \phi \\ \lambda^2 \\ \phi^2 \end{bmatrix} \tag{18}$$

$$\begin{bmatrix} \lambda \\ \phi \end{bmatrix} = \begin{bmatrix} \lambda_0 \\ \phi_0 \end{bmatrix} + \begin{bmatrix} \lambda_1 & \lambda_2 & \lambda_3 & \lambda_4 \\ \phi_1 & \phi_2 & \phi_3 & \phi_4 \end{bmatrix} \begin{bmatrix} s \\ l \\ s^2 \\ l^2 \end{bmatrix} \tag{19}$$

A priori values for equations (18) and (19) had initial accuracies at the 5–10 pixel level, sufficient to start the iteration process. The coefficients in equations (18) and (19) were continually updated as the evolving data processing produced more accurate parameter values, reducing the errors in the approximate transformation to a few pixel level. Once a location ϕ, λ was selected in a photomosaic, equation (18) would be used to compute which bands within all cubes contained this point to begin the image location measurement process. Hundreds to thousands of locations throughout the photomosaic were selected, with concentrations in the cube overlap areas to yield accurate THEMIS IR geometric and pointing parameters needed for precision map projection.

Figure 7 shows two Gale crater DIMs derived from the MOLA and HRSC DTMs where the higher spatial resolution HRSC DIM is on the right. Features measured in both the IR image cubes and the DIMs are called control points because their absolute locations (ϕ, λ, u) were determined precisely from the DIMs/DTMs. Their Mars-fixed positions were held as constants throughout the stereo photogrammetric reduction process, similarly as star positions are held as fixed/known parameters in an astrometric reduction process. To provide complete and redundant coverage over the 320 samples and thousands of lines in each band of all image cubes, and to precisely tie all bands together within a cube and between cubes, thousands of additional features only seen in the image cubes were measured and are referred to "tie" points. The tie point Mars-fixed positions were not known and were estimated in the stereo photogrammetric process. Airy-0 was one of these tie points. Selecting and measuring tie points are described later.

Control points were measured by producing a color image with the red channel being filled with the MOLA or HRSC DIM and the green and blue channels being filled with band 5 of an IR image (Figure 8). When the two data sets are not registered, the MOLA DIM appears as a red ghost image of the surface. By shifting the IR image in the blue and green channels with respect to the DIM in the red channel, the image becomes more grey as the two data sets become registered. The residual colors on the right after registration represent spatial resolution differences and actual surface thermal variations from the simple DTM-derived DIMs. Once registered, the IR s, l image coordinates become observables in the stereo photogrammetric process. The DIM image coordinates are used to compute the value of ϕ, λ for the control points from the sinusoidal map projection equations relating mosaic image location to Mars coordinates. These same DIM coordinates are used to extract the value of u from the associated DTM. For a tie point that was not identified in a DIM, usually because it was small relative to the DIM spatial resolution, its approximate DIM location was used to determine the approximate (a priori) values of ϕ, λ, u of the point. Then equation (18) was used to determine which other bands in all image cubes contained the control or tie point.

Once a control or tie point was identified, a 21×21 pixel^2 area surrounding the point was extracted from band 5 of a selected cube and used to make a 21×21 weighted digital Wiener filter [*Wiener*, 1949] to convolve with all bands in all cubes that contain the feature. The maximum output of the filter convolution

process was used to automatically measure the feature location, using interpolation to obtain locations to sub-THEMIS IR pixel resolution, and also used to compute a signal-to-noise ratio for the measured image location. Figure 9 shows a THEMIS tie point that was attempted to be measured in all bands of six different cubes. Only 46 *s*, *l* observation pairs were extracted as the control point went out of the field of view of some of the bands or the noise on the measured image location was too high to include in the stereo photogrammetric analyses.

Ideally, the convolution filter should be changed to reflect the differences in the spectral bands within an image cube and for the different lighting and viewing conditions between cubes. This was not done, simplified by the fact that the image cubes were all taken in nadir orientation and within a few hours of the same time of day. Even with the images changing between the spectral bands because of the surface thermal properties, the difference between the observed and predicted image locations was at the subpixel level, and therefore, no further work was needed to account for surface thermal properties.

The elimination of bad measurements had to be implemented in stages in order to not eliminate accurate measurements. In the early processing with a much smaller data set, measurements could appear to be bad when in reality the model parameters were not accurate. Therefore, as more and more measurements were added to the process and the parameter estimates became more accurate, tighter constraints were placed on defining bad measurements. The first step was to identify all potential measurement errors using the size of the postfit residuals, the differences between the measured and the computed image locations. Points with residuals larger than two pixels were remeasured if the measurement error was obvious; otherwise, the measurements were removed. Usually, the measurements that were removed had high image noise or the measured sample coordinates were outside of the 1–320 sample range. This first step removed all measurement blunders at the few pixel level.

To identify remaining bad measurement that were harder to identify by just looking at residuals, the pointing for each image cube was reestimated by removing one control or tie point at a time. The postfit residual measurement statistics of an image cube would improve by tens of percent or more when a single bad measurement was removed. These bad points were remeasured or deleted as before. This process was repeated by removing image location measurements from combinations of two points at a time in a cube since multiple measurement errors could have been made in a single cube. This process could identify when only one or two bands of a single cube were measured in error. After this process, the postfit residuals over the entire control and tie point data set were better than the one pixel level (1σ).

The final technique was to display the measured and predicted image locations as overlays on the images (Figure 9). The observed location is indicated by a "plus" and the predicted location as a "cross." Displaying all measurements in all bands and cubes together provided a powerful visual tool to identify measurement location discrepancies relative to the feature within the individual images. This display was also very useful in identifying measurement errors in noisy image bands or when the point was near the ends of a line. Once these measurements were corrected or removed, the differences between the measured and predicted image locations, referred to as residuals and measurement accuracies, were at the 1.5 pixel level for the MOLA control points and better than 0.3 pixels for the THEMIS tie points.

There were 89 MOLA control points and 501 THEMIS tie points in the Airy region, and there were 142 HRSC control points and 380 THEMIS tie points for Gale crater. One of the tie points was the crater Airy-0. There were 3942 *s*, *l* observations of the MOLA control points and 23,022 *s*, *l* observations of the THEMIS tie points to estimate 1562 tie point location and THEMIS IR parameters in the Airy-0 region. There were 8780 *s*, *l* observations of the HRSC control points and 21,222 *s*, *l* observations of the THEMIS tie points to estimate 1227 tie point location and THEMIS IR parameters in the Gale crater region. Parameter estimates were produced for the Airy-0 data set only, the Gale crater data set only, and the combined Airy-0 and Gale crater data sets. The solutions were iterated 4 times in the least squares parameter estimation process for all three cases. No change to the postfit residual statistics were seen after the third iterations, and a forth iteration was performed to verify this.

6. Results

6.1. Airy-0 Location

Four solutions were obtained for the location of Airy-0 from the Airy only and Airy-Gale combined data sets using both THEMIS IR geometric models 1 and 2. The four solutions varied by only 3 m on the Martian

Table 1. THEMIS IR Model 1 Parameter Values (Equations (10)–(13))

Parameter	A Priori	Airy	Gale	Airy + Gale	From K Terms
f_1 (mm)	200.000	202.953	202.707	202.844	202.756
f_2 (mm)	200.000	202.818	202.542	202.688	202.637
f_3 (mm)	200.000	202.586	202.335	202.464	202.444
f_4 (mm)	200.000	202.383	202.115	202.252	202.251
f_5 (mm)	200.000	202.197	201.913	202.057	202.058
f_6 (mm)	200.000	202.012	201.695	201.852	201.865
f_7 (mm)	200.000	201.817	201.493	201.654	201.672
f_8 (mm)	200.000	201.640	201.340	201.491	201.479
f_9 (mm)	200.000	201.452	201.142	201.298	201.294
f_{10} (mm)	200.000	201.259	200.949	201.105	201.101
f (mm)	200.000	204.370	204.312	204.792	204.790
α_1 (px mm^{-3})	0.000	0.000	0.000	0.000	0.000
α_1 (px mm^{-5})	0.000	0.000	0.000	0.000	0.000
b_1 (lines)	0.000	−0.560	−0.560	−0.560	−0.593
b_2 (lines)	0.000	−0.450	−0.450	−0.450	−0.414
b_3 (lines)	0.000	−0.250	−0.250	−0.250	−0.181
b_4 (lines)	0.000	−0.060	−0.060	−0.060	−0.022
b_5 (lines)	0.000	0.000	0.000	0.000	0.065
b_6 (lines)	0.000	−0.090	−0.090	−0.090	0.079
b_7 (lines)	0.000	−0.130	−0.130	−0.130	0.020
b_8 (lines)	0.000	−0.360	−0.360	−0.360	−0.111
b_9 (lines)	0.000	−0.480	−0.480	−0.480	−0.307
b_{10} (lines)	0.000	−0.700	−0.700	−0.700	−0.581

surface and had averaged Mars coordinates of $\phi = -5.07829°, \lambda = 0.00079°, u = 3393.134$ km. With 59.3 km/° on Mars, Airy-0 was 47 m east of the currently IAU-predicted prime meridian location. The formal covariance uncertainty of Airy-0 was at the 10 m level and with the postfit measurement residual statistics being 0.3 pixels (1σ), the 0.00079° or 47 m offset is boarder line to being statistically meaningful. These documented results will be provided to the MGCWG for them to determine updated parameter values in the Mars spin axis direction, spin rate, and prime meridian expressions to be recommended for adoption by the IAU WGCCRE.

Both models 1 and 2 were precise at the subpixel level, sufficient to produce seamless and 10-band aligned controlled photomosaics. Figure 10 shows band 5 in a 10-band-controlled photomosaic of Airy with the location of control and tie points overlain. Airy-0 is near the center and is identified as MED with a circled plus. It is seen that the control and tie points are well distributed with extra tie points in areas where cubes overlap along the north-south direction. Limited visual spot checks of the controlled photomosaic in overlap areas showed no misregistration, verifying to the precision of visual inspection that the mosaic was seamless.

6.2. THEMIS IR Models

The use of the 10 focal lengths f_i along each band, one focal length f across all bands and the 10 line biases b_i, a total of 21 geometric parameters in model 1 was sufficient to produce postfit image location

Table 2. THEMIS IR Model 2 Parameter Values (Equations (14) and (15))

Parameter	A Priori	Airy	Gale	Airy + Gale
f_k (mm)	200.000	203.942	203.918	203.931
K_{11} (mm/mm)	1.00000	0.99078	0.98938	0.99016
K_{12} (mm/mm)	0.00000	−0.00095	−0.00100	−0.00098
K_{13} (mm/mm^2)	0.00000	0.00074	0.00080	0.00077
K_{14} (mm/mm^2)	0.00000	−0.00005	−0.00000	0.00003
K_{15} (mm/mm^2)	0.00000	0.00006	0.00002	0.00004
K_{21} (mm/mm)	0.00000	−0.00257	−0.00229	−0.00260
K_{22} (mm/mm)	−1.00000	−1.00446	−1.00394	−1.00421
K_{23} (mm/mm^2)	0.00000	−0.00003	0.00002	0.00000
K_{24} (mm/mm^2)	0.00000	0.00015	0.00019	0.00017
K_{25} (mm/mm^2)	0.00000	−0.00107	−0.00109	−0.00108

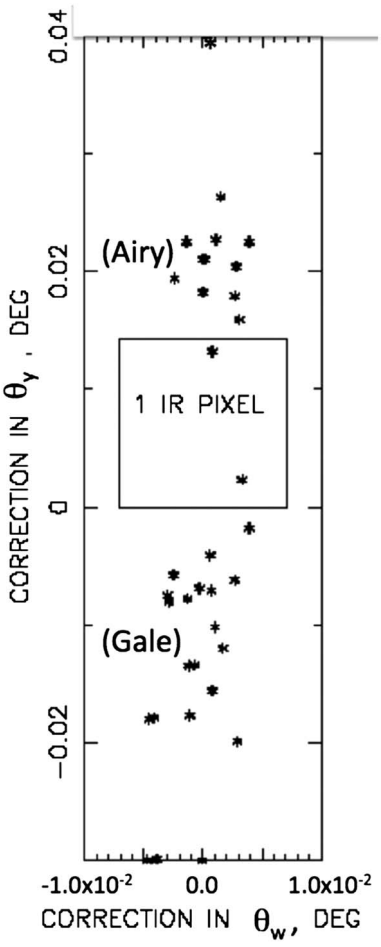

Figure 13. The postfit pointing corrections to the SPICE C kernels show the random pointing noise level of the 35 THEMIS IR cubes to be at the few hundredths of a degree. The few extreme pointing errors at the very top and bottom may be related to errors in the cube start time given in the cube label records. It is seen that the random pointing errors for Airy and for Gale fit within one IR pixel, but these two groups are separated by about two IR pixels.

measurement residuals at the subpixel level, but these residuals had systematic behaviors when compared to model 2 (Figure 11). It is seen that each band appears to be rotated with more rotation near the top and bottom of the IR detector and the rotation center is near the left of the IR detector at the top and bottom but moves toward the center near the central lines of the IR detector. The 21 geometric terms used in model 1 do not allow for such rotations. Therefore, model 2 was introduced to give this needed freedom. The postfit measurement statistics were about 0.3 pixels (1σ) for model 1 and were reduced to less than 0.2 pixels (1σ) using model 2 even though model 2 had only 11 parameters, K_{ij} and f.

The model 2 parameter values can be mapped into model 1 parameter values using

$$f_i = f_k K \left[K_{11} + K_{13}\, y\right] \tag{20}$$

where y is the IR detector coordinate of band "i" and

$$f = f_k K \left[K_{22} + K_{23}\, x\right] \tag{21}$$

where x is the IR detector coordinate associated with s. The b_i terms can be computed from the averages of the model differences along each band. As seen in Figure 11, these would be about 0.5 pixels at the top and bottom of the area array and are much less near the CCD center.

A comparison of the focal lengths is shown in Figure 12 using equations (20) and (21). Excellent agreement exists in all focal lengths. It is seen that model 2 gives the additional flexibility of having a varying focal length across the IR detector. The difference in focal length across the IR detector is only $\pm$ 0.3 mm, mapping to only 0.2 pixels at the ends of the bands.

The postfit THEMIS IR geometric parameter values for models 1 and 2 are listed in Tables 1 and 2, respectively. No optical distortion (α_1, α_2) was observed.

6.3. Spacecraft Attitude Reconstruction

The initial pointing values for the IR cubes were derived from NAIF SPICE "**C**" kernels, reconstructed from telemetered attitude orientation quaternions that had measurement errors at the hundredths of a degree level (Figure 13). Therefore, a correction to the pointing for each cube was computed, and the differences between these computed and predicted values were used to assess the random noise, or accuracy, of the **C** kernels. The average of all 35 pointing corrections were used to define $\theta_w, \theta_y, \theta_z$, while the differences between the actual pointing of each cube from the average were used to defined the random pointing noise. The pointing corrections after the average values for $\theta_w, \theta_y, \theta_z$ were applied to the **C** kernel through equation (7) are shown in Figure 13 where θ_w is across the orbit track and along the sample direction and θ_y is along the orbit track and the line direction. As previously mentioned, the time tag for the start of the image cube may be in error by a few lines that would be reflected in the θ_y correction.

The top cluster of 13 pointing corrections is for the IR cubes in the Airy region while the bottom cluster of 22 pointing corrections is for the IR cubes in the Gale region. Within both regions, as verified in Figure 13, the computed random pointing error is about 0.005° (3σ) cross track (θ_w) and about 0.01° (3σ) along track (θ_y), possibly somewhat larger due to a few time tag errors in cube start time at the very top and bottom of the figure. Pointing errors around the optical axis, θ_z, were also at the hundredth of a degree level but at this level had no effect on the results. The pointing noise increases slightly across track for the entire set of

Table 3. THEMIS IR Alignment Angles

Parameter	A Priori	Airy	Gale	Airy + Gale
θ_w (deg)	0.6720	0.6907	0.6892	0.6898
θ_y (deg)	90.0000	−90.0540	−90.0881	−90.0755
θ_z (deg)	0.0000	0.1727	0.1630	0.1667

35 cubes, but there is a distinct bias of about 0.03° or 2+ IR pixels along track between the two areas. The two data sets overlap in time with Airy covering from February 2003 to January 2006 and Gale covering from March 2002 to December 2010, so the bias in θ_y could not be related to a bias in the start times. The only notable differences are the different Mars regions (including DTMs)/orbital longitude between the two sites that may have different spacecraft thermal environments.

The individual pointing corrections were found to be valid for all bands within a cube, and there was no indication of high-frequency pointing jitter within a cube. Table 3 lists the values of the THEMIS IR alignment angles for Airy only, Gale only, and combined Airy-Gale, showing excellent agreement in θ_z and θ_w but the slight offset in θ_y between the two regions on Mars.

6.4. Conclusions

The completion of the MOLA global digital terrain model and the addition of the THEMIS IR and HRSC DTMs since the previous determination of the Airy-0 in 2001 location are excellent data sets upon which to base precision local and global stereo photogrammetric studies of Mars. The new location of Airy-0 determined in this analyses, 47 m east of its predicted location, was not statistically significant to warrant recommending a change to the Mars prime meridian epoch angle W_0. The geometric properties of the THEMIS IR were modeled to subpixel accuracy as demonstrated by the statistics of the observed minus predicted tie point image coordinate measurements (residuals) were 0.3 pixels (1σ) or better. The registration of THEMIS IR image areas to MOLA-derived DIMs using the color technique used here worked well, providing measurement residuals of 150 m (1σ) for absolute cartographic control. Displaying all of the observations of one point in all bands and in all cubes at the same time with the observed and predicted image locations overlain was crucial in the final identification of inaccurate measurements.

After iterating that the solution was complete and the postfit parameter values of control and tie point locations, THEMIS IR geometric parameters and THEMIS-fixed mounting alignment angles were used in equations (1)–(16), the remaining corrections to the ODY attitude/THEMIS pointing (*C* kernel) were random in the cross-track direction, having a variance of 0.005° (3σ), all within an IR pixel. The along-track pointing corrections fell within two groupings, one for the Airy crater IR cubes and one for the Gale crater IR cubes. The corrections within these two groups were within the size of the IR pixel, but the two groups were separated by two IR pixels. No explanation was found. It is possible that the registration of HRSC data with MOLA to produce the Gale crater DTM, using a different technique than the color registration technique used here, yielded the bias seen here, well within the MOLA spacing. However, one would expect to see such an offset in the cross-track direction where the MOLA spacing is much more.

The controlled THEMIS IR photomosaic of the Gale crater region was also used by the MGCWG to validate the accuracy of the cartographic map products being used by the Mars Surface Laboratory (MSL) flight team for their successful mission design and landing operations. Authors of this article, as individuals or members of the MGCWG, have provided this independent verification of cartographic map products used by the flight teams of Mars Pathfinder (MPF), the Mars Exploration Rovers, PHOENIX, and MSL. Other than MPF that was flown before MOLA and THEMIS, all other validations were based upon MOLA/THEMIS IR-derived map products using similar techniques described here.

It is believed by this analyses and similar analyses by the authors of other areas on Mars that the limit to absolute surface location accuracy on Mars is controlled by MOLA, having 300 m spacing in latitude and about 2 km spacing in longitude near the equator. It is not expected that any improvement in the absolute location accuracy of Airy-0 can be made using any image data set with MOLA, even those having higher spatial resolution than THEMIS IR. Therefore, improving the accuracy of predicting the orientation of the Mars surface in inertial space should be tied to current or future landers where Earth-based radiometric tracking can provide lander location accuracies at the meter level and give the most precise determinations of the Mars spin axis and spin rate as was done by *Konopliv et al.* [2011] and *Kuchynka et al.* [2014].

Acknowledgments
Appreciation is expressed to the MGS, ODY, and MEX flight operation teams and the MOLA, THEMIS, and HRSC science teams without whose efforts the data used in this article would not have been available. E. Wright and A. Maser of JPL configured the computer used for this analysis to use the NAIF SPICE toolkit and system of data kernels and the X-terminal image display tools. This work was supported by the NASA Science Mission Directorate 2001 Mars Odyssey Participating Scientist, the Mars Express Participating Scientist, and the Mars Data Analysis Programs.

References

Albee, A., and R. A. Arvidson (1991), The Mars global survey mission, *J. Geophys. Res.*, *56*(193), 119–120.
Acton, C. H. (1996), Ancillary data services of NASA's navigation and ancillary information facility, *Planet. Space Sci.*, *44*(1), 65–70.
Archinal, B. A., and M. Caplinger (2002), Mars, the meridian, and mert: The quest for Martian longitude, *Eos Trans. AGU*, *83*(47), Fall Meet. Suppl., Abstract P22D-06. [Available at http://abstractsearch.agu.org/meetings/2002/FM/sections/P/sessions/P22D/abstracts/P22D-06.html.]
Archinal, B. A., et al. (2011), Report of the IAU working group on cartographic coordinates and rotational elements: 2009, *Celest. Mech. Dyn. Astr.*, *109*(2), 101–135, doi:10.1007/s10569-010-9320-4.
Bierman, G. J. (1977), *Factorization Methods for Discrete Sequential Estimation, Math. in Sci. and Eng.*, 241 pp., vol. 128, Academic, New York.
Christensen, P. R., et al. (2004), The Thermal Emission Imaging System (THEMIS) for the Mars 2001 Odyssey mission, *Space Sci. Rev.*, *110*, 85–130.
de Vaucouleurs, G., M. E. Davies, and F. M. Sturms Jr (1973), Mariner 9 areographic coordinate system, *J. Geophys. Res.*, *78*, 4395–4404.
Duxbury, T. C., R. L. Kirk, B. A. Archinal, M. A. Caplinger, and G. A. Neumann (2002), *Mars Geodesy/Cartography Working Group Recommendations on Mars Cartographic Constants and Coordinate Systems, ISPRS,* vol. 34. part 4, Geospatial Theory, Processing and Applications, Ottawa. [Available at http://astrogeology.usgs.gov/search/details/Research/ISPRS/Duxbury/pdfforon-lineversion.]
Edwards, C., K. Nowicki, P. Christensen, J. Hill, N. Gorelick, and K. Murray (2011), Mosaicking of global planetary image datasets: 1. Techniques and data processing for Thermal Emission Imaging System (THEMIS) multi-spectral data, *J. Geophys. Res.*, *116*, E10008, doi:10.1029/2010JE003755.
Grotzinger, J. P., et al. (2012), Mars Science Laboratory mission and science investigations, *Space Sci. Rev.*, *170*(1–4), 5–56, doi:10.1007/s11214-012-9892-2.
Gwinner, K., J. Oberst, R. Jaumann, and G. Neukum (2010), Regional HRSC multi-orbit digital terrain models for the Mars Science Laboratory candidate landing sites, Abstract 2727 paper presented at 41st Lunar and Planetary Science Conference, Lunar and Planetary Institute, Houston, Tex.
Konopliv, A. S., S. W. Asmar, W. M. Folkner, O. Karatekin, D. C. Nunes, S. E. Smrekar, C. F. Yoder, and M. T. Zuber (2011), Mars high resolution gravity fields from MRO, Mars seasonal gravity, and other dynamical parameters, *Icarus*, *211*, 401–428.
Kuchynka, P., W. M. Folkner, A. S. Konopliv, T. Parker, S. Ryan, S. Park, S. Le Maistre, and V. Dehant (2014), New constraints on Mars rotation determined from radiometric tracking of the Opportunity Mars Exploration Rover, *Icarus*, *229*, 340–347, doi:10.1016/j.icarus.2013.11.015.
Malin, M. C., G. E. Danielson, A. P. Ingersoll, H. Masursky, J. Veverka, M. A. Ravine, and T. A. Soulanille (1992), The Mars observer camera, *J. Geophys. Res.*, *97*(E5), 7699–7718, doi:10.1029/92JE00340.
Neukum, G., et al. (2009), *HRSC: High Resolution Stereo Camera, Mars Express: The Scientific Investigations, ESA SP-1291*, ESA Publ. Div., Eur. Space Agency, Noordwijk, Netherlands.
Neumann, G., F. Lemoine, D. Rowlands, D. E. Smith, and M. T. Zuber (2001), Crossover analysis in MOLA data processing, *J. Geophys. Res.*, *106*(E10), 23,753–23,768.
Saunders, R. S., et al. (2004), 2001 Mars Odyssey mission summary, *Space Sci. Rev.*, *110*, 1–36.
Seidelmann, P. K., et al. (2002), Report of the IAU/IAG working group on cartographic coordinates and rotational elements of the planets and satellites: 2000, *Celest. Mech. Dyn. Astr.*, *82*, 83–110.
Semenov, B., C. Acton, N. Bachman, and E. Wright (2005), Reducing costs and managing and accessing navigation ancillary data using NASA's SPICE system.
Smith, D. E., et al. (2001), Mars Orbiter Laser Altimeter: Experiment summary after the first year of global mapping of Mars, *J. Geophys. Res.*, *106*(El0), 23,689–23,722.
Thompson, M. M. (1966), *Manual of Photogrammetry,* 3rd ed., Am. Soc. of Photogramm., Falls Church, Va.
Wiener, N. (1949), *Extrapolation, Interpolation, and Smoothing of Stationary Time Series*, Wiley, New York.
Yuan, D. N., W. L. Sjogren, A. S. Konopliv, and A. B. Kucinskas (2001), Gravity field of Mars: A 75th degree and order model, *J. Geophys. Res.*, *106*(E10), 23,377–23,401, doi:10.1029/2000JE001302.